First Uni-Traveling Carrier Photodiode Compact Model Enabling Future Terahertz Communication System Design

C. Mukherjee, P. Mounaix, C. Maneux
IMS Laboratory, University of Bordeaux
351, Cours de la Libération - 33405 Talence, France
chhandak.mukherjee@ims-bordeaux.fr

M. Natrella, J. Seddon, C. Graham, C. C. Renaud
Department of Electronic and Electrical Engineering,
University College London, London WC1E 7JE, U.K
c.renaud@ucl.ac.uk

***Abstract*—Monolithic optoelectronic integrated circuits (OEICs) are seen as key enabling technologies for future terahertz communications and upcoming beyond-5G networks. Co-design of monolithic OEICs requires computationally efficient compact models compatible with existing methodology/tool/design flow for timely and cost-effective realization of OEICs. This paper, inherently multidisciplinary, describes the first compact model for Uni-Traveling Carrier photodiodes (UTC PD), a key component for OEICs. Its equations capture the electronic transport and frequency response along with the photocurrent of the UTC PD under various applied optical power. It also dynamically computes the device junction temperature, accounting for self-heating effect. Excellent agreement between model and measurements as well as model scalability have been demonstrated.**

Keywords— Beyond-5G, Compact model, Optoelectronic integrated circuits, Terahertz communication, UTC- photodiode.

I. INTRODUCTION

With the growing demands of speed, next generation communication systems are required to cater to a wide range of applications such as social, medical, security, space and internet of things (IoT). When the minimum required bandwidth is expected to reach several tens of GHz, an even higher carrier frequency in the THz range (0.1–10 THz) is seen as the best potential solution [1]. With 'Beyond-5G' networks on the horizon, robust and intelligent system design is mandatory, which will be easy to manage, secure and able to support billions of devices. Anticipating the evolution of communications systems in the upcoming years (2020-2025) [1-2], heterogeneously integrated optoelectronic circuits are being seen as one of the key enabling terahertz technologies that are achievable through monolithic integration (Fig. 1 (a)). Such integration consists of photonic (such as UTC photodiodes) and electronic modules (such as trans-impedance amplifiers) on InP substrate along with the transmitting antenna in the same die, (Fig. 1 (b)), to minimize the losses as well as enhance the speed of operation as far as possible [3-4]. Thus, OEICs can support beyond 5G communications due to the cost-efficiency of on-chip integration, state-of-the-art photodiodes for photomixing, the speed and power-handling capacity of cutting-edge III-V electronics and high-directivity, power efficient antennas [1].

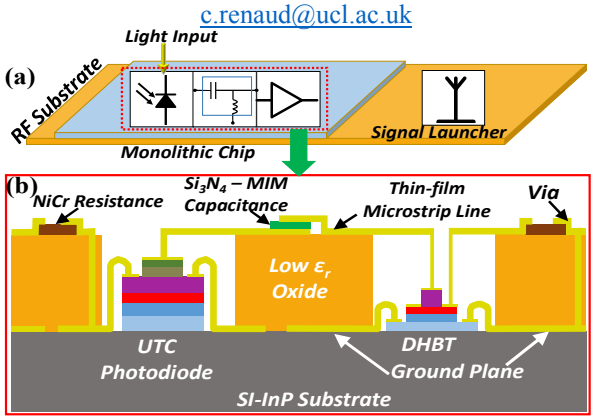

FIG. 1: (a) Schematic of Optoelectronic Monolithic chip; (b) Monolithic integration of the photodiode and the DHBT based amplifier on InP substrate.

UTC photodiodes operate on the separation principle of the absorption and the space charge region thereby allowing only photo-generated electron transport, thus overcoming the limitation of carrier transit time due to hole transport [5]. Hence, UTC photodiodes demonstrate better performance in speed and power handling than the conventional PIN photodiodes. In addition, the bandwidth of UTC photodiodes may reach a value greater than 600 GHz [4] thereby making them one of the most promising photomixing candidates for terahertz applications and OEICs [1, 3-4, 6]. Like all emerging technologies, design of such hybrid circuits requires computationally efficient as well as physics-based carrier transport models for both electrical and photonic parts. Additionally, it is mandatory to unify different multi-disciplinary (electronic, optical, thermal) aspects under one design environment using either additional design/software tools or a systematic assembly of existing software tools [7], to optimize design time and costs. At present, no such equivalent design tools/compact models truly exist for optoelectronics, despite the modelling efforts for UTC photodiodes [8-9].

As a first step towards developing a unified modelling solution, the first multi-physics and versatile Verilog-A compact model has been developed and validated for UTC-PDs, based on the equations of its carrier transport. The analytical model equations accurately capture electronic transport, frequency response and photocurrent behaviour under optical illumination. For simulation of thermal effects, especially at higher optical power and bias, the model

dynamically recalculates the internal device temperature to describe temperature dependence of the device characteristics using an additional fictitious node. Model validation has been performed on three available UTC-PD geometries and good model accuracy and scalability have been achieved under different bias, temperature and optical power conditions.

II. Analytical Model Development

In addition to basic diode physics, the model equations take into account the effect of optical power on the photo-current. Effectively, the total photocurrent expression is formulated based on the equations of carrier transport in UTC-PD [5, 10] while considering the DC photocurrent as a voltage dependent current source with the input optical power coupled at the light port as a voltage source. The equivalent circuit of UTC-PD is represented in Fig. 2 (a). In Fig. 2 (b), the UTC-PD structure is shown depicting different epitaxial layers and their layouts, while Fig. 2 (c) visualizes the equivalent circuit elements as well as different components of the diode current within the UTC-PD structure. The equivalent circuit is represented by the intrinsic diode consisting of the diode current source I_D and the junction capacitance C_{j0}. A shunt resistance R_{sh} is added in parallel to the diode to take into account the resistance of the reverse biased P-N junction. The DC photocurrent (as a function of the optical power) is added as a current source for the reverse bias operation of the photodiode under illumination. Finally, external elements, such as a series resistance is added to the anode terminal and parasitic inductances and capacitances are also introduced to account for the effect of the pads for dynamic simulation.

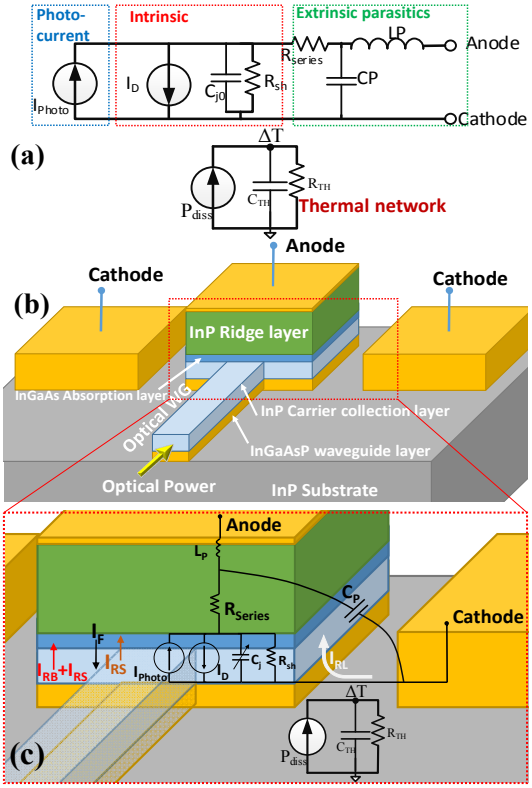

FIG. 2: (a) Equivalent circuit representation for the compact model; (b) Schematic of the UTC-PD; (c) elements of the equivalent circuit.

The behavior of a photodiode can be macroscopically described by,

$$I = I_S\left(e^{qV_d/k_BT} - 1\right) - I_{ph} \quad (1)$$

Where I_S is reverse saturation or dark current, V_d is the diode voltage and I_{ph} is the generated photocurrent. The first term on the right side of the equation is the conventional diode current, I_D. The basic diode equations based on the semiconductor physics are employed for describing the intrinsic diode behavior with the total diode current I_D represented by five components (Fig. 2 (c)):

$$I_D = I_F + I_{RS} + I_{RB} + I_{BV} + I_{RL} \quad (2)$$

I_F being the forward bias current is given as

$$I_F = Area \cdot J_S(T)\left[\exp\left(\frac{V_d}{NV_t(T)}\right) - 1\right], V_d > -5NV_t \quad (3)$$

Here N is the emission coefficient, J_S is the reverse saturation current (dark current) density, V_d is the applied forward bias across the photodiode and V_t is the thermal voltage. The reverse bias current has four components including the reverse saturation current I_{RS}, reverse breakdown current I_{RB} and I_{BV} and reverse leakage current I_{RL} that uses an expression similar to that of an interface generation leakage current in SOI PIN diodes [11]. Note that the temperature dependence of the parameters is included within the current equations. Also, all currents are defined in terms of current densities to make the model scalable. The individual expressions for the reverse current are as follows [12]:

$$\left.\begin{aligned} &I_{RS} = -Area \cdot J_S(T), V_d \le -5NV_t, \;\; I_{RB} = -I_{BV}, V_d = -BV, \\ &I_{BV} = -Area \cdot J_S(T)\left[\exp\left(-\frac{BV + V_d}{V_t(T)}\right) - 1\right], V_d < -BV \\ &I_{RL} = -Area \cdot J_R \cdot (T)^{1.5} \exp\left(-\frac{qE_g(T)}{2K_BT}\right) V_d^2 \sqrt{V_{bi} - V_d - V_t(T)}, V_d < V_{ref} \end{aligned}\right\} \quad (4)$$

Here, BV is the reverse breakdown voltage, and E_g is the bandgap of the InGaAs absorption layer, V_{bi} is the junction built-in potential and V_{ref} is the threshold value of reverse bias that governs the dominance of the component I_{RL}. The depletion/junction capacitance of the photodiode is written as,

$$C_{dep} = Area \cdot C_{j0}(T)\left(1 - \frac{V_d}{V_j(T)}\right)^{-M} \quad (5)$$

With C_{j0} being the zero bias junction capacitance, V_j being the junction potential and M being the grading coefficient of the P-N junction. The temperature effects in model parameters such as C_{j0}, J_S and V_j have also been taken into account. Besides, the temperature dependence of the energy gap E_g has to be taken into account as well.

Additionally, the expression for the photocurrent, I_{photo}, is formulated as an external current source in parallel to the diode current, I_D, which is controlled by the input optical or impinging power, P_{opt}. First, the optical power in dBm (P(light)dBm) is converted into watts to be used within the model. Next, the DC photocurrent density, J_{ph}, is modeled by, $J_{ph} = P_{opt} \times \text{Responsivity/Area}$, Where, the *Responsivity* is a measure of the external quantum efficiency of the photodiode, measured in A/W. While *Responsivity* is a function of the wavelength, however, for model simplicity we have kept it as

a model parameter, since we have always used a wavelength of 1.55 μm, corresponding to the minimum wavelength dispersion widely used in fiber optic communication. We have also normalized the photocurrent with respect to the diode area to incorporate photocurrent scalability. The total photocurrent density can be essentially written using three components, J_1, J_2 in the absorber layer and J_3 in the collection layer that can be written as [10],

$$\left.\begin{aligned} J1 &= J_{ph}\frac{W_A}{W_A+W_C}\frac{1}{1+j\omega\tau_A}, \quad J2 = -J1\left(1-\frac{q\mu_n n_0 E_{ind}}{J_{ph}}\right)\frac{j\omega\tau_R}{1+j\omega\tau_R} \\ J3 &= J_{ph}\frac{W_C}{W_A+W_C}\frac{1}{1+j\omega\tau_A}\sin(\omega\tau_C/2)\frac{\exp(-\omega\tau_C/2)}{\omega\tau_C/2} \end{aligned}\right\} \quad (6)$$

Where, W_A and W_C are widths of the absorber and collection layers, respectively, which are used as model parameters. τ_A is the electron travelling time and τ_R is the dielectric relaxation time in the absorption layer, whereas τ_C is the transit time in the collection layer. E_{ind} is the self-induced field in the absorption layer responsible for change in electron transport from diffusive to drift, μ_n is the electron mobility and n_0 is photo-generated minority electron concentration. The time constants, τ_A, τ_C and τ_R can be written as [5],

$$\tau_A = \frac{W_A^2}{3D_n}+\frac{W_A}{v_{th}}, \quad \tau_C = \frac{W_C}{v_{sat}}, \quad \tau_R = \frac{\varepsilon_s}{q\mu_h p_0} \quad (7)$$

Where, D_n is the diffusion coefficient of electron, v_{th} is the thermal velocity in the absorption layer, v_{sat} is the saturation velocity in the collection layer, μ_h is the hole mobility and p_0 is the doping hole density in the absorption layer. The final expression of the photocurrent used in the model is given as,

$$I_{photo} = Area\cdot(J1+J2+J3) \quad (8)$$

Finally, to take into account the effect of dynamic self-heating at high electrical power and temperature as well as high optical power, we have incorporated an additional thermal node in the equivalent circuit (Fig. 2 (b)) that dynamically calculates the junction temperature as a function of the bias conditions as well as intrinsic temperature using the thermal resistance, R_{TH}. A thermal capacitance, C_{TH}, is also used in the equivalent circuit to represent the dynamic behavior of thermal impedance. This is of high importance for improving the model accuracy at more extreme operating conditions (temperature rise in 150-250°C range) due to high inherent heat dissipation in the UTC-PDs. The calculation of the junction temperature, T_j, uses the following expressions,

$$T = T_j = T_{dev} + R_{TH}P_{diss}, \quad \text{with } Pdiss = I_{Total}V_d \quad (9)$$

The temperature dependence of the thermal conductivity has also been taken into account in the UTC-PD compact model. The expression of the junction temperature in (9) is used to dynamically recalculate the temperature dependence of all model parameters at different operating bias conditions.

III. Model Validation

Model validation was done using UTC-PD measurements performed at the ultrafast photonics laboratory at the University College London. Three UTC-PD geometries were used with active areas of 3×15, 4×15 and 7×15 μm^2. The epitaxial structure of the UTC-PDs has a 120 nm thick p-doped $In_{0.53}Ga_{0.47}As$ absorption and a 300 nm thick n-doped InP collection layer [13]. Initial DC and S-parameter measurements were performed on unilluminated UTC-PDs at three different temperatures (15, 25 and 35ºC) under different forward and reverse bias conditions. Fig. 3 shows I-V characteristics of the three geometries of the UTC-PDs in the forward and reverse bias operating conditions measured at 15, 25 and 35ºC (temperature is maintained using a Peltier system). Excellent model accuracy and scalability as well as temperature dependence of model parameters can be observed. Note that under reverse operating conditions, for a more accurate description of the UTC-PD behavior, the leakage current equation in (4) is essential.

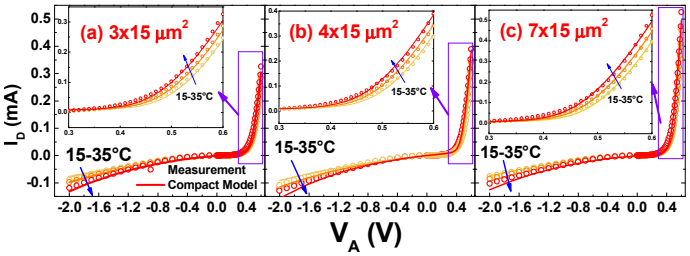

FIG. 3: Scalable model comparison: I-V characteristics of UTC-PDs with areas (a) 3×15 (b) 4×15 and (c) 7×15 μm^2. Inset: Forward operating regime.

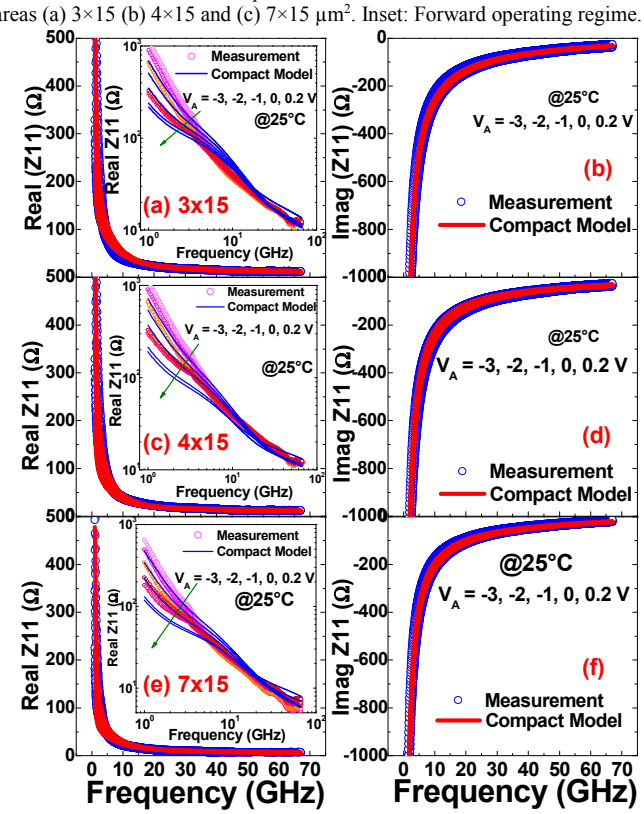

FIG. 4: Measured (symbol) and simulated (line) input impedance (Z11) showing its real (a)-(c) and imaginary parts (d)-(f).

The one-port S-parameter (S11) up to a frequency of 67 GHz is measured for the three UTC-PD geometries from which the input impedance Z11 is extracted. Due to the absence of de-embedding structures, Short-Open-Load calibrations were done till the probe tips and the effect of the pad parasitics were taken into account by introducing the series resistance, R_{series}, and the parasitic inductance and capacitance, L_P and C_P, into

the external sub-circuit of the model. The real and imaginary parts of the one port Z-parameter, *i.e.* the input impedance, Z11, extracted from S-parameter measurements, are shown in Figs. 4 (a)-(f) for the three UTC-PD geometries. The real part represents the resistance and the imaginary part represents the capacitive reactance of the input impedance of UTC-PDs. Note that the asymptotic nature of the real part at higher frequencies converges to the series resistance value, typically 5-10 Ω, whereas the reactance becomes more inductive at higher frequencies. The developed compact model accurately describes these effects and it accurately simulates the input impedance of the UTC-PD for the entire frequency range for all the geometries. A good description of the bias-dependence and scalability of the depletion capacitance is captured in the model in the entire bias range used.

Next, the measurements carried out with the UTC-PDs under illumination for a wide range of optical power (6 to 15 dBm) are validated against the UTC-PD compact model results. The illumination of the UTC-PDs was done using a CW Laser wavelength 1.55 µm (linewidth 100 kHz) guided through an optical fiber and focused through a lens at the end of the fiber. The optical signal is focused on the absorption layer of the UTC-PD through the optical wave guide (trench) fabricated on the sides of the test structures. Adjustment of the fiber position was done to obtain maximum photocurrent intensity for each optical power. Fig. 5 compares the simulated and measured photocurrents for all geometries under optical powers in the range 6 to 15 dBm. The model simulation shows an excellent agreement between the measurement and simulation at all reverse bias voltages and optical powers for all geometries, owing to the physical description of UTC-PD photocurrent through analytical eqs. (6)-(8).

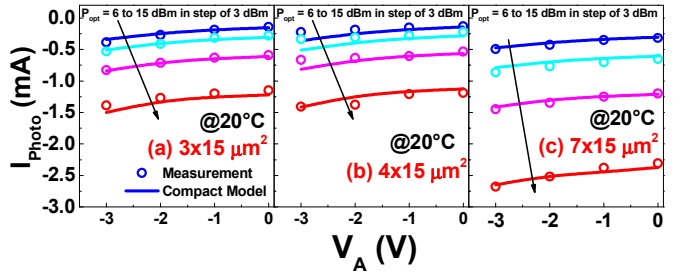

FIG. 5: Scalable model comparison: Measured (symbol) and simulated (line) photocurrent of UTC-PDs geometries (a) 3×15 (b) 4×15 and (c) 7×15 µm².

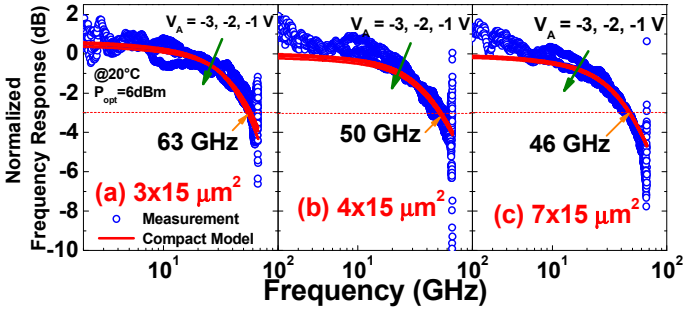

FIG. 6: Measured (symbol) and simulated (line) frequency response of UTC-PDs with area (a) 3×15 (b) 4×15 and (c) 7×15 µm² at optical power of 6 dBm.

The measured frequency responses of the UTC-PDs at a P_{opt} of 6 dBm are compared to model simulation in Fig. 6 for the three UTC-PD geometries. Excellent agreement is also observed in this case. Moreover, the 3 dB cut-off frequencies are also well described by the model. Since the 3 dB cut-off frequency is an indicator of the UTC-PD bandwidth, the values are coherent with the UTC-PD area: larger area implies bigger capacitance thus increasing the RC delay product and thus resulting in a smaller bandwidth. These results are in very good agreement with the results reported in [19].

IV. Conclusions

In this work we report the first electrical compact model for UTC-PDs. The compact model is developed based on the UTC-PD transport physics and the model equations accurately capture the behavior of the photocurrent as a function of the optical power and temperature. Model scalability is also demonstrated which is essential for circuit designers. Moreover, the developed verilog-A compact model is fully compatible with commercial electronic circuit simulation tools, and thus facilitates a single simulator based co-designing of photo-electronic systems. This marks the first step towards realizing a unified and holistic (electronic, photonic, thermal) design environment for optoelectronic monolithic integrated circuits which will ultimately aid designers of next generation communication technologies.

References

[1] T. Nagatsuma, G. Ducournau, and C. C. Renaud, "Advances in terahertz communications accelerated by photonics", *Nat. Photonics*, vol. **10**, pp. 371–379, 2016.

[2] R. Waterhouse and D. Novack, "Realizing 5G: Microwave Photonics for 5G Mobile Wireless Systems", *IEEE Microwave Magazine*, vol. **16** (8), pp. 84-92, 2015.

[3] A. J. Seeds, H. Shams, M. J. Fice and C. C. Renaud, "TeraHertz Photonics for Wireless Communications", *J. Lightwave Technology*, vol. **33**, pp. 579-587, 2015.

[4] H.-J. Song and T. Nagatsuma, *Handbook of Terahertz Technologies: Devices and Applications*. *Pan Stanford USA*, April 15, 2015, ISBN: 9789814613088.

[5] T. Ishibashi, S. Kodama, N. Shimizu and T. Furuta, "High-Speed Response of Uni-Traveling-Carrier Photodiodes", *Jpn. J. Appl. Phys*., vol. **36**, pp. 6263-6268, 1997.

[6] C. C. Renaud, M. Natrella, C. Graham, J. Seddon, F. Van Dijk and A. J. Seeds, "Antenna Integrated THz Uni-Traveling Carrier Photodiodes", *IEEE Journal of Selected Topics in Quantum Electronics*, vol. **24** (2), pp. 1-11, 2018.

[7] C. Mukherjee, B. Ardouin, J.Y. Dupuy, V. Nodjiadjim, M. Riet, T. Zimmer, F. Marc and C. Maneux, "Reliability-Aware Circuit Design Methodology for Beyond-5G Communication Systems", *IEEE Trans. Device and Materials Reliability,* vol. **17**, pp. 490-506 2017.

[8] M. Natrella, C.-P Liu., C. Graham, F. van Dijk, H. Liu, C. C. Renaud, and A. J. Seeds, "Modelling and measurement of the absolute level of power radiated by antenna integrated THz UTC photodiodes", *Opt. Express*. Vol. **24**, pp. 11793-11807, 2016.

[9] M. Natrella, C.-P. Liu, C. Graham, F. van Dijk, H. Liu, C. C. Renaud and A. J. Seeds, "Accurate equivalent circuit model for millimetre-wave UTC photodiodes", *Opt. Express*. Vol. **24**, pp. 4698-4713, 2016.

[10] T. Ishibashi, T. Furuta, H. Fushimi, S. Kodama, H. Ito, T. Nagatsuma, N. Shimizu and Y. Miyamoto, "InP/InGaAs uni-traveling carrier photodiodes", *IEICE Trans. Electron*. Vol. **E83-C**, pp. 938–949, 2000.

[11] A. Schmidt, S. Dreiner, H. Vogt, A. Goehlich and U. Paschen, "Analytical model for thin-film SOI PIN-diode leakage current", *Solid-State Electron*. Vol. **130**, pp. 4-8, 2017.

[12] M. E. Brinson and S. Jahn, "Qucs: A GPL software package for circuit simulation, compact device modelling and circuit macromodelling from DC to RF and beyond", *Int. J. Numer. Model*, vol. **22**, pp. 297-319, 2009.

[13] A. J. Seeds, C. Renaud and M. Robertson, "Photodetector including multiple waveguides", *United States patent* **US7851782** (B2) (2010).